research papers

Iron speciation in ancient Attic pottery pigments: a non-destructive SR-XAS investigation

Fabrizio Bardelli,[a] Germana Barone,[b] Vincenza Crupi,[c] Francesca Longo,[c] Giacomo Maisano,[c] Domenico Majolino,[c]* Paolo Mazzoleni[b] and Valentina Venuti[c]

[a]Institut des Sciences de la Terre (ISTerre), Maison de Geosciences, 1381 rue de la Piscine, 38400 Grenoble, France, [b]Geological Science Department, University of Catania, Corso Italia 57, 95129 Catania, Italy, and [c]Physics Department, University of Messina, V. le F. Stagno D'Alcontres 31, 98166 Messina, Italy. E-mail: majolino@unime.it

The present work reports a detailed investigation on the speciation of iron in the pigments of decorated pottery fragments of cultural heritage relevance. The fragments come from the Gioiosa Guardia archaeological site in the area of the 'Strait of Messina' (Sicily, Southern Italy), and date back to VI–V century BC. The purpose of this study is to characterize the main pigmenting agents responsible for the dark-red coloration of the specimens using non-destructive analytical techniques such as synchrotron radiation X-ray absorption spectroscopy (SR-XAS), a well established technique for cultural heritage and environmental subjects. Absorption spectra were collected at the Fe K-edge on the Italian beamline for absorption and diffraction (BM8-GILDA) at the European Synchrotron Radiation Facility in Grenoble (France). In order to determine the speciation of Fe in the samples, principal component analysis and least-squares fitting procedures were applied to the near-edge part of the absorption spectra (XANES). Details on the local structure around the Fe sites were obtained by analyzing the extended part of the spectra (EXAFS). Furthermore, an accurate determination of the average Fe oxidation state was carried out through analysis of the pre-edge peaks of the absorption spectra. Samples resulted composed of an admixture of Fe_2O_3 (hematite or maghemite) and magnetite (Fe_3O_4), occurring in different relative abundance in the dark- and light-colored areas of the specimens. The results obtained are complementary to information previously obtained by means of instrumental neutron activation analysis, Fourier transform infrared absorbance and time-of-flight neutron diffraction.

Keywords: XANES; EXAFS; XRF; ancient decorated pottery; non-destructive analysis; pigmentation; iron.

1. Introduction

A large variety of chemical, spectroscopic and microscopic techniques are currently employed in the field of cultural heritage to study a variety of artifacts, from paintings and sculptures to ancient pottery (Klein et al., 2004; Chen, 2006; Rampazzi et al., 2007; Feathers et al., 2006; Shortland et al., 2007; Barilaro et al., 2008a,b). Recently, techniques based on the use of synchrotron radiation (Tang et al., 2001; Chiari et al., 2003; Dooryhée et al., 2004; Cotte et al., 2005; Young et al., 2006; Kockelmann et al., 2006; Chalmin et al., 2006; Mazurier et al., 2006) achieved a relevant role thanks to their intrinsically non-destructive character, a fundamental property when dealing with archaeological artifacts. High brilliance, mono-chromatic and collimated synchrotron X-ray beams are invaluable tools for examining fragile, valuable and/or unique artifacts with minimal or no damage. Among the investigations performed exploiting synchrotron radiation, recent studies (Padovani et al., 2006; Barilaro et al., 2007; Pradell et al., 2008; Reiche & Chalmin, 2008; Arletti et al., 2008; Crupi et al., 2010; Bardelli et al., 2011a) have shown that X-ray absorption spectroscopy (XAS) is a powerful and flexible technique for archaeological artifacts. It provides quantitative information on the local and electronic structure (oxidation state, number and nature of closest neighbors, atomic distances, structural disorder and site symmetry) of a selected element. Compared with X-ray diffraction (XRD), XAS does not require long-range-ordered structures and can therefore be applied to amorphous (or even liquid) systems. In addition, contrary to XRD, XAS, being a resonant technique, can be

used on diluted or trace elements embedded in complex matrixes, adsorbed on surfaces or incorporated in a host phase. XAS measurements can be performed in air and they virtually do not require restrictions on the type and size of the sample, which can be metallic or insulating, rough or polished, solid or liquid. These properties are particularly important in the archaeological field, in which samples are precious artifacts made of different materials and where the elements responsible for the color can be present at high diluted levels.

In a previous work (Barilaro et al., 2008b) a detailed characterization of the ceramic body of the same samples studied in the present work was performed combining destructive micro-analyses, such as INAA (instrumental neutron activation analysis) and FTIR (Fourier transform infrared) absorbance, and non-destructive techniques, such as TOF-ND (time-of-flight neutron diffraction). The presence and/or variations in the content of some minerals suggested the existence of different workshops. In particular, the TOF-ND analysis showed different amounts of calcite, confirming the FTIR results. The presence of newly formed minerals, namely gehlenite and diopside, detected by both techniques, allowed the firing temperature to be estimated. Since gehlenite occurs at ∼923 K and starts to turn to diopside at ∼1173 K, these mineral phases give a clear indication of the firing technology used in the manufacture (Capel et al., 1985; Riccardi et al., 1999). In particular, the simultaneous presence of both minerals in the investigated samples indicates that a firing temperature of ∼1173 K was used and suggests a similar manufacture for the ceramic body. The differences detected in the mineralogical composition allowed the classification of the samples into two main sub-groups: on one side samples having a composition typical of the Greek production, on the other side samples exhibiting a composition that can be ascribed to a Western production. In addition, the FTIR investigation, preliminarily performed on the decorated surface of the specimens, showed a higher amount of clay and iron oxides with respect to the inner bulk, suggesting the typical Greek red-figured decoration process.

The red-figured pottery appears in Greece around 530 BC and, with respect to the black-figured style, is characterized by an inversion of the colors: the scenes are depicted in red on a black background and the details and the edges of the images (or part of them) are highlighted by black lines, allowing the artists to develop the study of perspective and human anatomy. The pottery samples studied in this work come from the Sicilian (Southern Italy) archaeological site of Gioiosa Guardia, located in the 'Strait of Messina' area (Fig. 1). This excavation area, situated on the Tyrrhenian coast of Sicily, revealed a housing continuity from the prehistoric to the classical age. A wide part of the Greek built-up area, lying on the rest of two previous settlements dating back to the ancient Bronze and Iron Ages, were brought to light during recent excavations. A large variety of artifacts were found and
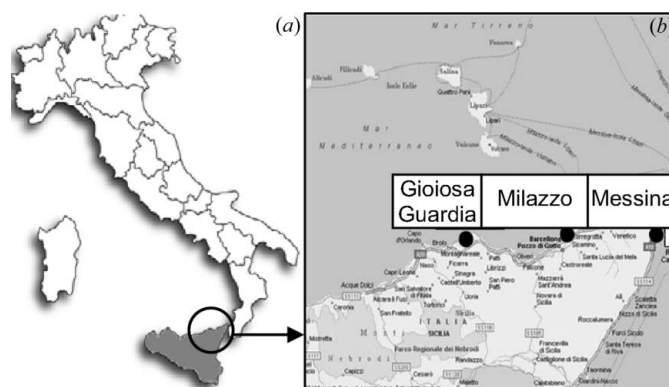

Figure 1
(a) Map of Italy; Sicily is shaded gray and the archaeological excavation area is indicated by a circle. (b) Magnification showing the location of the archaeological site of Gioiosa Guardia.

assigned to the most recent housing period (VI–V century BC). The red pictures of two representative pottery fragments selected from the above-mentioned set and showing similar macroscopic characteristics were chosen. Since, in the studied specimens, iron-bearing compounds are believed to be mainly responsible for the pigmentation, the present work is focused on the determination of the speciation of Fe.

An accurate characterization of the artifacts can contribute to the understanding of ancient manufacturing techniques, distribution of the production areas, use of artefacts in the past, as well as to the commercial and human exchanges between contemporary cultures. In addition, the information obtained can be of great help in determining the best conservation and/or restoration method.

2. Experimental

2.1. Samples

The specimens studied in this work are two fragments of pottery from a wider set of findings from the Gioiosa Guardia archaeological site dated back to VI–V century BC (see Fig. 2). A trace-element analysis was carried out by INAA (Barilaro et al., 2008b) on the same fragments allowing us to assign both of them to the Greek (Attic) productions sub-group according to the typical Cr and Ni contents. In the following the fragments will be labeled GI27-D(L) and GI30-D(L), where the suffix 'D' or 'L' will indicate analyses performed on the dark- or light-colored regions of the specimens, respectively.
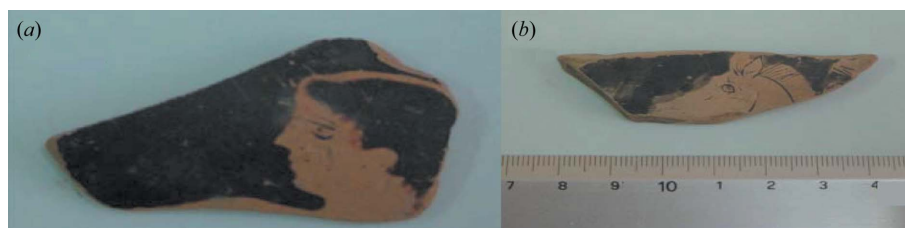

Figure 2
Photographs of fragment GI-27 (a) and GI-30 (b).

research papers

2.2. Experimental set-up and data treatment

Synchrotron radiation XAS (SR-XAS) measurements were performed at the Fe K-edge (7112 eV) on the Italian beamline (BM8-GILDA) (Pascarelli *et al.*, 1996) at the European Synchrotron Radiation Facility in Grenoble (France). The beamline optics include a fixed-exit monochromator equipped with a pair of Si 311 crystals and a sagittal dynamic focusing system, which resulted in a beam intensity on the sample of about 1×10^{10} photons s^{-1} and a beam spot size of 200 μm (horizontal) and 150 μm (vertical). A couple of Pd-coated mirrors are used for efficient harmonic rejection. Considering the monochromator crystals and the vertical aperture of the main slits (1 mm), the energy resolution at the Fe edge is estimated to be about 0.4 eV. Samples were mounted in a large vacuum chamber, which was evacuated down to $\sim 10^{-5}$ mbar, and positioned at 45°/45° geometry with respect to the incoming X-ray beam and the fluorescence detector. An energy-resolving solid-state (high-purity Ge) 13-element detector (ORTEC), suitable for diluted elements, was used to acquire the fluorescence yield from the samples. The set of iron reference compounds included metallic Fe foil, FeO, Fe_2O_3, Fe_3O_4, $FeCl_3$, $Fe(NO_3)_3$ and $FeSO_4$. All reference compounds spectra were acquired in transmission geometry, measuring the beam upstream and downstream of the sample with ionization chambers. A reference Fe foil was mounted in a second experimental chamber and measured simultaneously to the reference compounds for accurate energy calibration. Energy calibration of archaeological samples was performed by measuring the Fe foil before and after each scan, to ensure detection of unphysical energy shifts.

Absorption spectra were collected in the range 6900–7900 eV for Fe, corresponding to 14 Å^{-1} in the wavevector space (k). Quantitative information on samples speciation was obtained applying principle component analysis (PCA) and least-squares fitting (LSF) to the XANES spectra. These are well established procedures useful to help determine the speciation of a large class of materials (Bardelli *et al.*, 2011*b*; Ressler *et al.*, 2000; Frenkel *et al.*, 2002). In particular, PCA can be used to decompose a set of data files into the minimum number of components needed to describe the largest variations of the data. These primary, or principal, components are those which contain the signal and are sufficient to reconstruct each of the experimental spectra in some linear combination, while other components in the system refer to the noise. The aim of this procedure is to determine how many components or reference spectra are needed to describe the set of data files. PCA supplements the traditional approach through a global view of speciation within the entire series of spectra. Furthermore, target transformation procedure can be applied to the reference spectra in the attempt to determine whether a chosen reference spectrum (*i.e.* from a given model compound) can be considered as a legitimate 'end-member' component. Mathematically, this means that it can be represented in the same projected space defined by the components of the sample spectra. This is done by multiplying the reference spectrum by the eigenvector column and row matrix. If this resultant spectrum matches well with the reference (within 1%) then the reference spectrum is a possible species in the unknown data sets. The results from PCA offer constraints that can then be applied to the traditional nonlinear least-squares analysis. On the other hand, LSF consists of fitting the experimental spectra of the samples with a linear combination of the set of reference compounds spectra suggested by PCA. This procedure can give an estimation (within 10–15%) of the relative abundance of the selected candidates in the experimental data. It is worth noting that these procedures only give consistent results if the reference set chosen is sufficiently representative of the composition of the samples. PCA and LSF were performed using the *SIXPACK* and *IFEFFIT* packages, respectively (Webb, 2005; Newville, 2001). The average oxidation state of the samples was calculated from the study of the pre-edge peaks of the absorption spectra as described by Wilke *et al.* (2001) and Waychunas *et al.* (1983). Wilke *et al.* (2001) demonstrated that, at the Fe K-edge, the relevant parameter for estimation of the oxidation state is not the energy position of the absorption edge (conventionally taken as the first peak of the first derivative of the absorption spectrum) but the position of the centroid of the pre-edge peaks, which are related to $1s$–$3d$/$4d$ electronic transitions. The centroid position was calculated for the reference iron oxides of known oxidation state and the calibration curve obtained was used to estimate the oxidation state of the samples spectra.

Local structure around iron was obtained by refining the extended X-ray absorption fine structure (EXAFS) analysis up to the third coordination shell (about 3.5 Å). These parameters were compared with the structures of the selected reference compounds. Standard procedures were used for the extraction of the EXAFS signal $\{\chi(k) = [\mu(k) - \mu_0(k)]/\mu_0(k)\}$ from the raw absorption data $[\mu(E)]$. Raw spectra were subtracted from the pre-edge background and normalized on the high-energy side of the curve (>200 eV from the edge); this allowed the comparison of samples with different absorber content. Accurate energy calibration was performed on each scan using the spectrum of iron foil acquired before and after each energy scan.

Minimizations were performed in the Fourier back-transformed wavevector space, *i.e.* filtering out contributions from noise and coordination shells higher than about 3.5 Å. Both the extraction of the EXAFS signal and the least-square minimizations were performed using a Fortran-written software package (*ESTRA-FITEXA*; Bardelli *et al.*, 2009) based on the *MINUIT* routines from CERN libraries (James & Roos, 1975). The errors on the structural parameters were obtained from the *MINOS* subroutine belonging to the *MINUIT* package, which also takes into account the correlation between free parameters. The *ATOMS* (Ravel, 2001) package was used to generate the atomic clusters centered on the absorber atom to be used as reference structures for calculating theoretical amplitude and phase back-scattering functions with the *FEFF8* package (Ankudinov *et al.*, 1998).
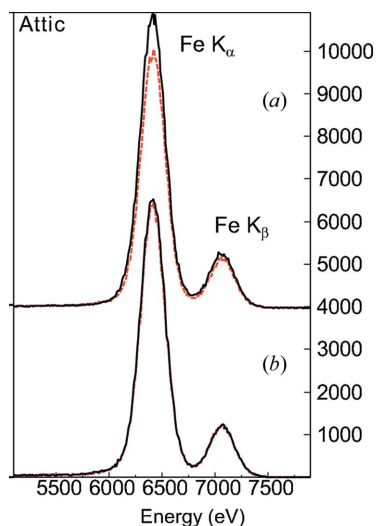
Figure 3
XRF spectra of light (L, solid lines) and dark (D, dashed lines) portions of GI-27 (*a*) and GI-30 (*b*) fragments showing the Fe K_α (6405 eV) and K_β (7059 eV) fluorescence emission. Note that the amount of iron in the dark and light portion is similar.

Figure 4
Left panel: example of the procedure used to isolate and fit the pre-edge peaks: subtraction of a modified arctangent function mimicking the absorption-edge step, and fit using one or more Gaussian functions. Right panel: calibration curve obtained through a linear fit of the pre-edge peaks centroid position of iron oxides of known oxidation state ($Fe^{2+}O$, $Fe_3^{2.66+}O_4$, $Fe_2^{3+}O_3$, triangles) and used to estimate the oxidation state of the studied samples (crosses). The spectra corresponding to the colored areas of the samples (D) have oxidation states close to 2.7, while that of the light-colored areas (L) are close to 3.0.

3. Results and discussion

3.1. SR-XRF analysis

Preliminary X-ray fluorescence spectra using synchrotron radiation on several dark (D) and light (L) portions of each fragment were acquired with the aim of identifying the main elements present. The fluorescence signal indicated that iron is present in all samples and is by far the most concentrated element. XRF spectra showing the $K\alpha$ and $K\beta$ emission lines of iron are reported in Fig. 3. The information that can be gathered from the XRF spectra is only qualitative; nevertheless, it is worth noting that the amount of iron in the dark and light portions of both samples is similar.

Fluorescence spectra were acquired at 7.2 keV, thus elements heavier than iron were not detected. Another limitation concerns elements lighter than potassium that cannot be detected owing to their low X-ray absorption cross section and to the presence of a Be window reducing the fluorescence from light elements. The fact that we did not detect calcium, although calcite was clearly identified as one of the main phases in a previous neutron diffraction study (Barilaro *et al.*, 2008c), can be ascribed to the limited probe depth of X-rays (a few tens of micrometers) compared with neutrons (millimeters), and is an indication of the difference between the surface and the bulk composition of the samples investigated.

3.2. XANES analysis

The average oxidation state was estimated following the method described by Wilke *et al.* (2001). The pre-edge peak was isolated by subtracting a curve which mimics the absorption edge (a modified arctangent), and the peaks were fitted using one or more Gaussian functions (Fig. 4). The centroids of the pre-edge peaks were calculated by averaging the positions of the f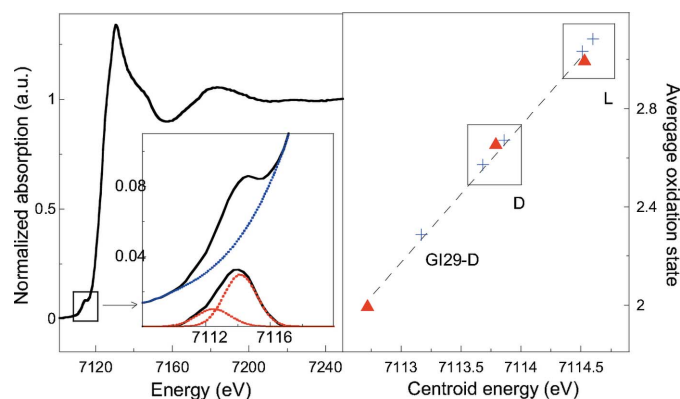itted peaks weighted for their height. This method was first applied to the spectra of the reference iron oxides of known oxidation state (FeO, Fe_3O_4, Fe_2O_3) in order to construct a centroid position *versus* oxidation-state calibration curve. The calibration curve was then applied to obtain the oxidation states of the samples from the position of their centroids. Considering the uncertainty on the determination of the centroid position (0.1–0.2 eV), the overall uncertainty on the determination of the oxidation-states values is estimated to be about 0.1–0.2. The calibration curve and the oxidation-state values of the samples are reported in the right-hand panel of Fig. 4 and the numerical values in Table 2. For the light-colored regions (L) of the studied samples the oxidation states are close to 3 (the value of the Fe_2O_3 standard), suggesting a preponderance of the Fe(III) species. The dark-colored regions (D) have average oxidation states of 2.6–2.7, *i.e.* close to that of the Fe_3O_4 mixed-valence reference oxide (2.66), suggesting the presence of magnetite or compounds with lower Fe oxidation state. The values of the oxidation states obtained from the LSF procedure, described in the following, are also reported in Table 2, and are in good agreement with those obtained from pre-edge analysis.

XANES spectra of the samples and of the reference standards are reported in the right- and left-hand panels of Fig. 5, respectively. The spectra collected on the light-colored regions (GI27-L and GI30-L) are very similar, as are the spectra acquired on the dark-colored areas (GI27-D and GI30-D), suggesting a similar Fe speciation in the respective dark- and light-colored areas.

PCA was applied to the XANES spectra, revealing that two components are necessary to satisfactorily reconstruct the samples spectra. This is confirmed by the values of the indicator function (*IND*; Malinowski, 1980), which has a minimum in correspondence to two components, and from the values of the variance, which rapidly drop down after the two components. Target transformation procedure suggested Fe_2O_3

research papers

Table 1
Goodness-of-fit values for the target transform procedure.

χ^2 is the traditional sum of the squared differentials, whereas the R value is a measure of the percent misfit. The values indicate that hematite (Fe_2O_3) and magnetite (Fe_3O_4) have the best matches, while $FeCl_3$ and $Fe(NO_3)_3$ are still possible candidates for least-square fits. The blank line highlights the cut off for the statistical parameters, which indicate that the compounds below the blank line (FeO, metallic Fe, $FeSO_4$) are not suitable candidates.

Target	r ($\times 10^3$)	χ^2
Fe_2O_3	0.3	0.34
Fe_3O_4	0.8	0.72
$FeCl_3$	1.9	1.62
$Fe(NO_3)_3$	2.2	1.94
FeO	7.6	6.11
Fe	16.7	13.1
$FeSO_4$	27.1	23.4

Table 2
Relative concentrations of Fe_3O_4 and Fe_2O_3 as obtained from the LSF procedure.

Also reported is the concentration sum, which is close to 100% for all samples, and the goodness-of-fit value (χ^2), both indicating good matches to the experimental spectra. The values of the oxidation states obtained from the pre-edge analysis are reported in the last columns and compared with the values obtained by the linear combination of the oxidation states of the reference oxides (Fe_3O_4 and Fe_2O_3), weighted for their relative concentrations. The error on the concentrations is 10–15% and that on the oxidation state is 0.1–0.2.

Sample	Fe_2O_3 (%)	Fe_3O_4 (%)	Total	χ^2 ($\times 10^4$)	Oxidation state Pre-edge	Oxidation state LSF
GI27-L	56	47	103	1.4	3.0	2.9
GI30-L	72	30	102	1.8	3.1	3.0
GI27-D	24	75	99	8.2	2.7	2.7
GI30-D	28	73	101	11.7	2.6	2.8

(hematite or maghemite) and Fe_3O_4 (magnetite) as the best candidates among the set of standard compounds. The results of the target transform procedure on all the reference standards measured are reported in the left-hand panel of Fig. 6. Note the excellent agreement between the Fe_2O_3 and magnetite, while $Fe(NO_3)_3$ and FeO resulted in poorer matches, but are still acceptable candidates. On the contrary, all other references are in very poor agreement with the corresponding transformed spectrum, as confirmed by the statistical values (R and χ^2) reported in Table 1. Further evidence of the validity of the selected candidates is that the inclusion of Fe_2O_3 and Fe_3O_4 in the PCA run does not increase the number of components necessary to reconstruct the samples spectra.

Least-square fitting, i.e. fits of the samples spectra using a weighted linear combination of the spectra of the reference standards, was performed using combinations of a maximum of three standards indicated as acceptable candidates in the PCA step [Fe_2O_3, Fe_3O_4, $Fe(NO_3)_3$ and FeO]. In final refinements the $Fe(NO_3)_3$ and FeO standards were removed as they

were found to have negligible contribution in the LSF. The spectra of the samples and the corresponding fit curves are reported in the right-hand panel of Fig. 5, and the numerical values, including the parameters indicating the goodness of the fits, are reported in Table 2. The results clearly show that the ratio Fe_3O_4 and Fe_2O_3 is reversed in the dark-colored regions (D) with respect to the light-colored ones (L). In particular, the D regions of the samples are composed of a preponderant amount of magnetite, while in the L regions the main iron species is Fe_2O_3, according to the analysis of the oxidation states.

3.3. EXAFS analysis

Structural refinements were performed in the k^2-weighted back-Fourier-transformed space (back-transform window 0.5–3.4 Å, uncorrected for phase shift), up to $k = 12$ Å^{-1}. The back-Fourier transforms of the samples and reference
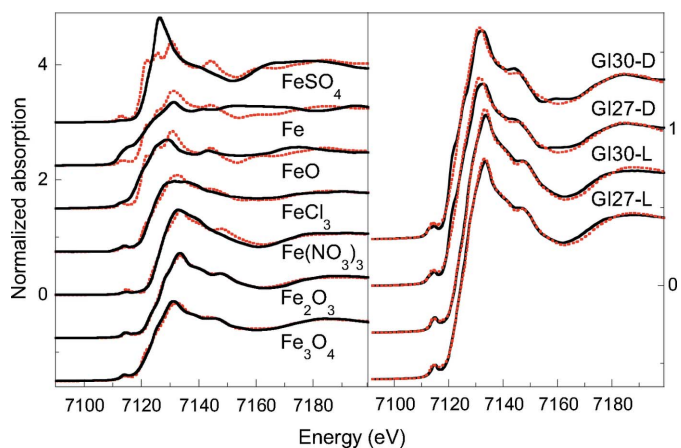
Figure 5
Left panel: normalized absorption spectra of the reference standards (solid lines) and target transformation (dashed lines). Right panel: LSF of the archaeological samples spectra performed using a linear combination of the Fe_3O_4 and Fe_2O_3 spectra (solid lines: experimental data; dashed lines: fit curves). The spectra are vertically shifted for ease of view.
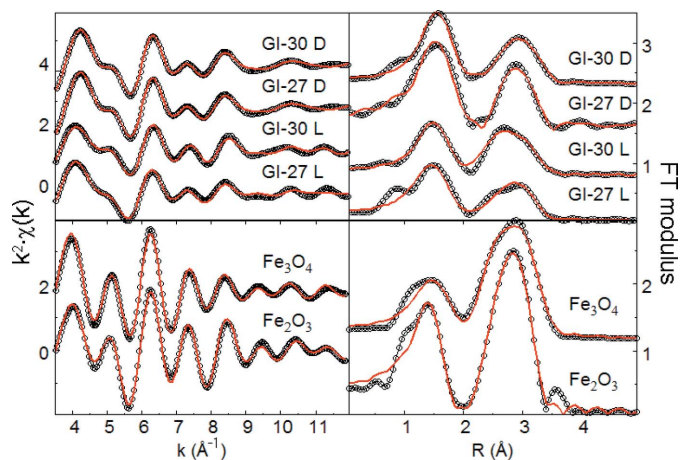
Figure 6
Left panels: k^2-weighted EXAFS signal and fit curves of the spectra of the artifacts (top) and selected reference compounds (bottom). Fits were performed in the back-transformed k-space in the range 3.5–12 Å^{-1}. Right panels: Fourier transforms of the EXAFS signals and fit curves reported in the left panels (not corrected for phase shift). In both panels points represent the experimental data and solid lines the fit curves. The spectra are vertically shifted for easy of view.

compounds are reported in the left-hand panels of Fig. 6 with the corresponding fit curves superimposed. The Fourier transforms (FTs) of the samples and reference standards and the corresponding fit curves are reported in the right-hand panels of Fig. 6. The FT is proportional to a radial distribution function centered on the absorber atom (Fe). This means that each peak corresponds to a specific atomic distance or to the convolution of more distances (owing to the limited resolution, which depends on the extension of the spectra in the k space). The real atomic distances are obtained by applying theoretical phase functions while fitting the experimental data to the EXAFS model function.

The first peak in the FT is attributed to the first coordination shell and arises from Fe–O contributions. Further peaks, up to about 3.5 Å (uncorrected for phase shift), are assigned to Fe—Fe contributions. The refinements were performed assuming that the observed structures arise from a linear combination of the reference compounds structures in the same relative abundance as obtained by the LSF. To avoid strong correlations with the Debye–Waller (σ^2) and the EXAFS amplitude reduction factor (S_0^2), the coordination numbers were set to the crystallographic values of the iron oxides references weighted for the values of their relative concentrations obtained from LSF. To further reduce the correlation between parameters, global parameters, such as S_0^2 and the energy shift (not reported), were optimized through first-shell analyses and kept fixed in the final refinements. Only atomic distances and Debye–Waller factors were allowed to be free to vary in the final refinements. The maximum number of free parameters, eight, never exceeded the number of independent points, $(2\Delta R \Delta K)/\pi \simeq 13$. The theoretical resolution for spectra extending to $k = 12$ Å^{-1} (the useful extension of the data acquired) is $\pi/(2k_{max}) \simeq 0.1$ Å.

The reference oxides were fitted by fixing the coordination numbers (CNs) to their crystallographic values and the distances were grouped taking into account the limited resolution of XAS (0.1 Å) (CNs for magnetite were grouped considering its spinel nature, *i.e.* an admixture of tetrahedral and octahedral iron sites in a 1:2 ratio).

The values of the refined structural parameters are reported in Table 3 together with those of the reference iron oxides. Light portions (L) have a first coordination shell of O atoms centered at about 1.92 Å, in good agreement with the Fe$_2$O$_3$ standard. On the contrary, dark portions (D) resulted in a slightly longer first oxygen coordination shell (1.96 Å), which is compatible with the larger amount of Fe$_3$O$_4$ revealed by LSF. In all samples two Fe—Fe coordination shells are detected: a first one roughly at 3.00 Å and a second one at ~3.45 Å. The local structure observed in the samples is compatible with a structure arising from an admixture of the selected reference oxides. Nevertheless, it has to be noted that taking into account the uncertainty on the relative proportions of Fe$_2$O$_3$ and Fe$_3$O$_4$ retrieved by LSF, which reflects in large errors on the coordination numbers, and the fact the local structure around the iron sites of Fe$_2$O$_3$ and Fe$_3$O$_4$ largely overlaps (also due to limited resolution of XAS), it is difficult to find a marked difference between the local structure of the

Table 3
Structural parameters of the archaeological samples and selected reference oxides obtained from the refinement of the EXAFS signals.

Coordination numbers (CN) of reference oxides were kept fixed to their crystallographic values and averaged while closer than 0.1 Å to account for the lower resolution of XAS. CN of samples spectra were kept fixed to the values calculated from the linear combination of that of the reference oxides, weighted by the relative concentration retrieved by the LSF procedure. The numbers within parentheses represent the error on the last digit.

	Path	CN	R (Å)	σ^2 ($\times 10^3$) (Å^2)	S_0^2
Sample					
GI27-L	Fe—O	5.8	1.92 (3)	11 (5)	0.6 (1)
	Fe—Fe	4	3.00 (6)	19 (9)	
	Fe—Fe	4.5	3.45 (5)	12 (6)	
GI30-L	Fe—O	5.9	1.92 (3)	7 (4)	0.5 (2)
	Fe—Fe	4	2.98 (3)	8 (5)	
	Fe—Fe	3.5	3.46 (4)	5 (3)	
GI27-D	Fe—O	5.4	1.96 (2)	8 (3)	0.6 (1)
	Fe—Fe	4	3.01 (5)	18 (7)	
	Fe—Fe	7.5	3.48 (4)	14 (5)	
GI30-D	Fe—O	5.3	1.95 (2)	7 (4)	0.6 (1)
	Fe—Fe	4	3.05 (4)	15 (7)	
	Fe—Fe	8	3.52 (5)	17 (6)	
Standard					
Fe$_2$O$_3$	Fe—O	6	1.92 (2)	10 (4)	0.7 (2)
	Fe—Fe	4	2.97 (4)	6 (2)	
	Fe—Fe	3	3.45 (2)	2 (1)	
Fe$_3$O$_4$	Fe—O	5.3	1.99 (2)	14 (4)	0.9 (2)
	Fe—Fe	4	2.97 (2)	10 (3)	
	Fe—Fe	8	3.47 (2)	5 (3)	

light and dark regions of the samples. The values of the amplitude reduction factors are lower than those of the reference compounds. This could be ascribed to the self-absorption effect (Zschech *et al.*, 1992), which is due to the energy dependence of the X-ray penetration depth and is enhanced by particular matrix compositions (*i.e.* a thick layer of iron embedded in a light matrix). Finally, the Debye–Waller factors for the Fe—Fe coordination shells are larger than those of the reference standards, reflecting in second peaks with reduced intensity with respect to the standards (Fig. 6, left-hand panels). This is an indication of the presence of a strong static disorder, probably arising from poorly crystallized or amorphous iron phases.

4. Conclusions

In this work, decorated pottery fragments of cultural heritage relevance coming from the Gioiosa Guardia archaeological site belonging to the 'Strait of Messina' area (Sicily, Southern Italy), and dating VI–V century BC, were investigated. X-ray absorption spectroscopy revealed that the samples are constituted by an admixture of iron oxides (Fe$_2$O$_3$ and Fe$_3$O$_4$). In particular, the dark pigment corresponded to a larger amount of magnetite (Fe$_3$O$_4$), while, in the light-colored areas, Fe$_2$O$_3$ was the preponderant iron species. The values of the average oxidation states and the local structure around the iron sites confirm this scenario. In addition, EXAFS analysis suggested the presence of poorly crystalline or amorphous iron phases, which could be the reason why such phases were

Fabrizio Bardelli *et al.* • Iron speciation in ancient Attic pottery pigments

not detected in previous studies involving X-rays or neutron diffraction techniques.

The observed variations in the relative abundance of Fe_2O_3 and magnetite in the dark-colored regions could be related to variations in the thickness of the pigmented layer: for lower thicknesses the fluorescence from the underlying Fe_2O_3 contributes more to the overall signal, resulting in an increased Fe_2O_3 to Fe_3O_4 ratio.

The results of the present work showed the co-presence of the Fe(II) oxide (in the form of hematite or maghemite) and the mixed-valence iron oxide (magnetite), which are well known to be the basis of many inorganic pigments widely used since the antiquity, such as the red-ochre. The presence of iron oxides confirms the results of the FTIR absorbance measurements (Barilaro *et al.*, 2008b). Nevertheless, because of the overlapping of bands and/or peaks characteristic of other mineralogical phases in the same absorbance region, it was not possible to unambiguously distinguish the iron phases present in the specimens.

It is worth remembering that the oxidation product of Fe_3O_4 (magnetite) is either γ-Fe_2O_3 or α-Fe_2O_3 depending on the oxidation temperature and/or, possibly, on the crystallite size of the starting magnetite. This information can be linked to the firing process, which consists of oxidation, reduction and final re-oxidation steps, leading to the conclusion that in the dark and light portions of the fragments part of magnetite is transformed into maghemite or hematite.

Finally, the fact that both specimens analyzed in this study led to very similar results is a strong indication that the same manufacturing process was used to decorate the ceramic surface.

References

Ankudinov, A. L., Rave, B., Rehr, J. J. & Conradson, S. D. (1998). *Phys. Rev. B*, **58**, 7565–7576.

Arletti, R., Vezzalini, G., Quartieri, S., Ferrari, D., Merlini, M. & Cotte, M. (2008). *Appl. Phys. Mater. Sci. Process.* **92**, 127–135.

Bardelli, F., Barone, G., Crupi, V., Longo, F., Majolino, D., Mazzoleni, P. & Venuti, V. (2011a). *Anal. Bioanal. Chem.* **399**, 3147–3153.

Bardelli, F., Cattaruzza, E., Gonella, F., Rampazzo, G. & Valotto, G. (2011b). *Atmos. Environ.* **45**, 6459–6468.

Bardelli, F., Meneghini, C., Mobilio, S., Ray, S. & Sarma, D. D. (2009). *J. Phys. Condens. Matter*, **21**, 195502.

Barilaro, D., Barone, G., Crupi, V., Majolino, D., Mazzoleni, P., Tigano, G. & Venuti, V. (2008a). *Vib. Spectrosc.* **48**, 269–275.

Barilaro, D., Crupi, V., Interdonato, S., Longo, F., Maisano, G., Majolino, D., Venuti, V., Barone, G., Mazzoleni, P., Tigano, G., Imberti, S. & Kockelmann, W. (2008b). *Nuovo Cimento C*, **31**, 371–388.

Barilaro, D., Crupi, V., Majolino, D., Venuti, V., Barone, G., D'Acapito, F., Bardelli, F. & Giannici, F. (2007). *J. Appl. Phys.* **101**, 064909.

Barilaro, D., Crupi, V., Majolino, D., Venuti, V., Barone, G., Tigano, G., Imberti, S. & Kockelmann, W. (2008c). *J. Phys. Condens. Matter*, **20**, 104254.

Capel, J., Huertas, F. & Linares, J. (1985). *Mineral. Petrogr. Acta*, **29**, 563–575.

Chalmin, E., Vignaud, C., Salomon, H., Farges, F., Susini, J. & Menu, M. (2006). *Appl. Phys. Mater. Sci. Process.* **82**, 213–218.

Chen, M. L. (2006). *Archaeometry*, **48**, 565–580.

Chiari, G., Giustetto, R. & Ricchiardi, G. (2003). *Eur. J. Mineral.* **15**, 21–33.

Cotte, M., Dumasb, P., Richard, G., Breniaux, R. & Walter, Ph. (2005). *Anal. Chim. Acta*, **553**, 105–110.

Crupi, V., Majolino, D., Venuti, V., Barone, G., Mazzoleni, P., Pezzino, A., La Russa, M. F., Ruffolo, S. A. & Bardelli, F. (2010). *Appl. Phys. A*, **100**, 845–853.

Dooryhée, E., Martinetto, P., Walter, Ph. & Anne, M. (2004). *Radiat. Phys. Chem.* **71**, 863–868.

Feathers, J. K., Holliday, V. T. & Meltzer, D. J. (2006). *J. Archaeol. Sci.* **33**, 1651–1665.

Frenkel, A. I., Kleifeld, O., Wasserman, S. R. & Sagi, I. (2002). *J. Chem. Phys.* **116**, 9449–9456.

James, F. & Roos, M. (1975). *Comput. Phys. Commun.* **10**, 343–367.

Klein, M., Jesse, F., Kasper, H. U. & Gölden, A. (2004). *Archaeometry*, **46**, 339–356.

Kockelmann, W., Siano, S., Bartoli, L., Visser, D., Hallebeek, P., Traum, R., Linke, R., Schreiner, M. & Kirfel, A. (2006). *Appl. Phys. Mater. Sci. Process.* **83**, 175–182.

Malinowski, E. R. (1980). *Anal. Chim. Acta*, **122**, 327–330.

Mazurier, A., Volpato, V. & Macchiarelli, R. (2006). *Appl. Phys. Mater. Sci. Process.* **83**, 229–233.

Newville, M. (2001). *J. Synchrotron Rad.* **8**, 322–324.

Padovani, S., Borgia, I., Brunetti, B., Sgamellotti, A., Giulivi, A., D'Acapito, F., Mazzoldi, P., Sada, C. & Battaglin, G. (2006). *Appl. Phys. Mater. Sci. Process.* **83**, 521–528.

Pascarelli, S., Boscherini, F., D'Acapito, F., Hrdy, J., Meneghini, C. & Mobilio, S. (1996). *J. Synchrotron Rad.* **3**, 147–155.

Pradell, T., Molera, J., Smith, A. D. & Tite, M. S. (2008). *J. Archaeol. Sci.* **35**, 2649.

Rampazzi, L., Campo, L., Cariati, F., Tanda, G. & Colombini, M. P. (2007). *Archaeometry*, **49**, 559.

Ravel, B. (2001). *J. Synchrotron Rad.* **8**, 314–316.

Reiche, I. & Chalmin, E. (2008). *J. Anal. At. Spectrom.* **23**, 799–806.

Ressler, T., Wong, J., Roos, J. & Smith, I. L. (2000). *Environ. Sci. Technol.* **34**, 950–958.

Riccardi, M. P., Messiga, B. & Duminuco, P. (1999). *Appl. Clay Sci.* **15**, 393–409.

Shortland, A., Rogers, N. & Eremin, K. (2007). *J. Archaeol. Sci.* **34**, 781–789.

Tang, C. C., MacLean, E. J., Roberts, M. A., Clarke, D. T. & Pantos, E. (2001). *J. Archaeol. Sci.* **28**, 1015–1136.

Waychunas, G. A., Apted, M. J. & Brown, G. E. Jr (1983). *Phys. Chem. Miner.* **10**, 1–9.

Webb, S. M. (2005). *Phys. Scr.* **T115**, 1011–1014.

Wilke, M., Farges, F., Petit, P. E., Brown, G. E. Jr & Martin, F. (2001). *Am. Mineral.* **86**, 714–730.

Young, M. L., Casadio, F., Schnepp, S., Almer, J., Haeffner, D. R. & Dunand, D. C. (2006). *Appl. Phys. Mater. Sci. Process.* **82**, 163–168.

Zschech, E., Troger, L., Arvanitis, D., Michaelis, H., Grimm, U. & Barerschke, K. (1992). *Solid State Commun.* **82**, 1–5.